THE JOURNAL OF PHYSICAL CHEMISTRY LETTERS
A JOURNAL OF THE AMERICAN CHEMICAL SOCIETY

Open Access
This article is licensed under CC-BY 4.0

pubs.acs.org/JPCL
Letter

Unveiling the Phase Transformation Mechanism in BN from Large-Scale Machine Learning Molecular Dynamics

Jaeyoung Cho, Nikhil Rampal,* Stephen E. Weitzner, Graeme Henkelman, and Liwen F. Wan*

Cite This: J. Phys. Chem. Lett. 2026, 17, 13353−13360
Read Online

ACCESS | Metrics & More | Article Recommendations | Supporting Information

ABSTRACT: Boron nitride (BN) exhibits rich polymorphism, including cubic, hexagonal, rhombohedral, and wurtzite phases, whose dynamic transformations govern the stability and performance of BN-based materials in modern electronics, quantum photonics, and energy devices. Despite their technological importance, the atomistic mechanisms underlying its phase evolution remain poorly understood. Here, we use large-scale molecular dynamics simulations with a MACE-based machine learning interatomic potential. The potential is trained on high-fidelity density functional theory data and validated against *ab initio* molecular dynamics simulations to investigate phase transformation pathways in crystalline BN. We identify a layer-by-layer transformation mechanism that is initiated at heterogeneous BN interfaces, where local structural reconstruction propagates into neighboring crystalline regions. We further show that the transformation propensity depends on the interfacial structure and crystallographic orientation. These results provide atomistic insight into BN phase transformations under diverse thermodynamic conditions, while the associated MACE training workflow offers a generalizable framework for studying phase transformation mechanisms in other complex materials.

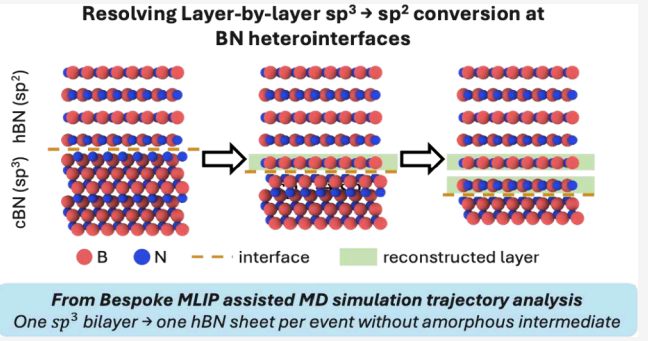

Boron nitride (BN) is a III−V compound known for its structural versatility and wide range of technological applications. It exists in several polymorphic forms, including cubic (cBN), hexagonal (hBN), rhombohedral (rBN), and wurtzite (wBN), each exhibiting distinct structural, mechanical, thermal, and electronic properties. This polymorphism makes BN an important material for applications spanning solid-state electronics, high-performance abrasives, thermal management, two-dimensional heterostructures, and quantum photonics.[1−3] Consequently, understanding the dynamical phase stability and transformation mechanisms of BN has become increasingly important.

The technological performance of BN is closely tied to its phase composition and structural evolution. For example, in lithium−metal batteries, ultrathin hBN membranes have emerged as promising protective coatings for Li-metal anodes because of their superior chemical inertness, mechanical strength, and impermeability, which help suppress dendrite growth and parasitic interfacial reactions.[4] Similarly, the exceptional hardness of cBN supports its widespread use in wear-resistant cutting tools, while its high thermal conductivity makes it an attractive filler for heat-dissipating electronic composites.[5] More broadly, the development of tunable, defect-tolerant BN coatings requires precise control over phase composition, crystallographic orientation, and interfacial stability, all of which are governed by the atomistic mechanisms underlying the dynamic evolution of BN polymorphs.[6]

The phase transformation behavior of BN has frequently been interpreted by analogy with carbon, particularly the graphite-to-diamond transition. Within this analogy, the hBN-to-cBN transformation has long been regarded as the counterpart of the graphite-to-diamond phase transition.[7] However, a growing body of experimental and computational evidence has revealed important limitations of this analogy. Unlike carbon, BN possesses polar B−N bonds and anisotropic interlayer interactions coupled with significant van der Waals forces, resulting in transformation pathways and phase stability regimes that differ fundamentally from those of carbon.[8,9] These characteristics necessitate detailed investigation of how heterogeneous interfaces, crystallographic orientation, and local structural compatibility influence reconstructive transformations between competing bonding networks. In particular, recent studies suggest that cBN may remain thermodynamically stable at atmospheric pressure up to approximately

Received: August 29, 2026
Revised: November 2, 2026
Accepted: November 3, 2026
Published: November 10, 2026



ACS Publications
© 2026 The Authors. Published by American Chemical Society

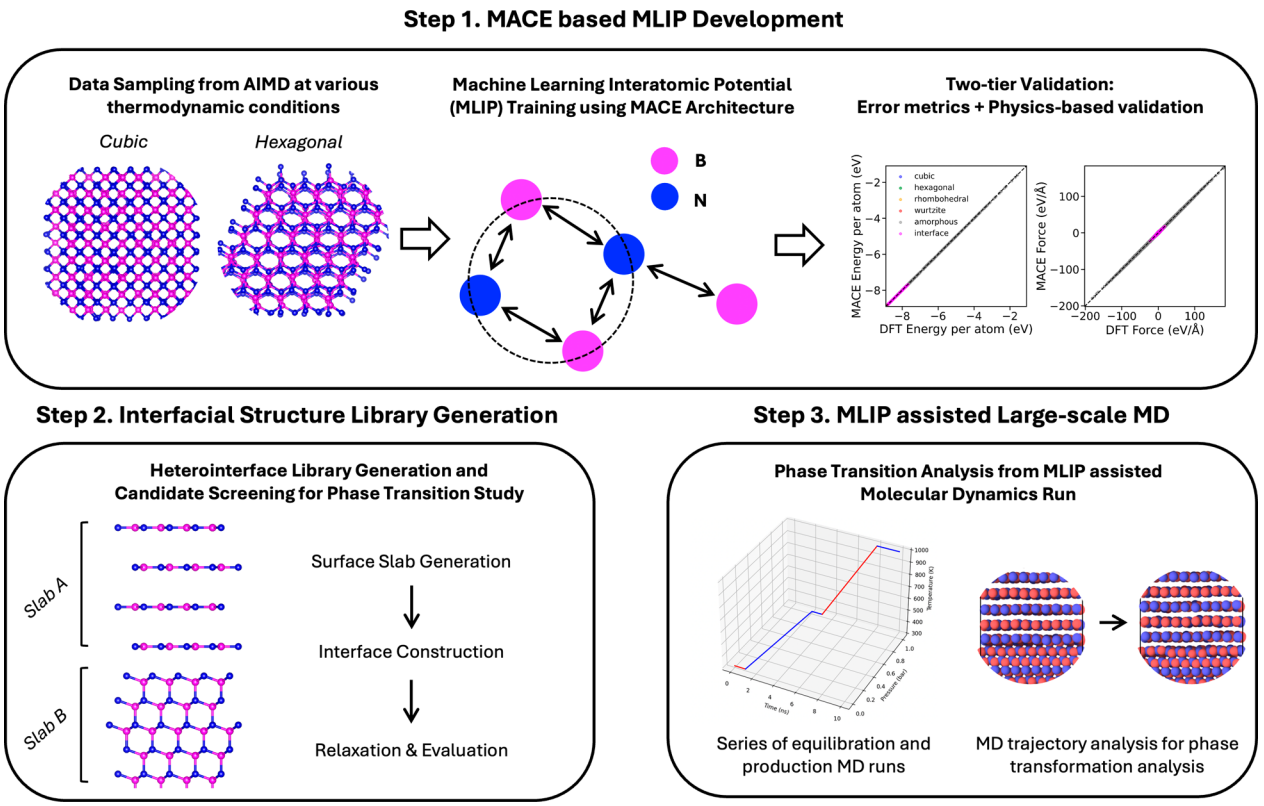

Figure 1. Overall workflow for MACE-based machine learning interatomic potential (MLIP) development and its application to investigate interfacial phase transformation pathways in BN. In step 1, a MACE MLIP is trained using AIMD-generated configurations spanning diverse BN polymorphs, including cubic, hexagonal, rhombohedral, wurtzite, amorphous-like phases and interfacial structures. Model hyperparameters (l_{max} and the number of channels) are optimized, and the resulting MLIP is validated through a two-tier strategy consisting of (i) standard energy and force parity metrics and (ii) physics-based validation against AIMD reference data using radial distribution functions (RDFs) and vibrational power spectra. In step 2, a library of BN interfacial structures is constructed through surface slab generation, interface matching, and structural relaxation for subsequent screening. In step 3, large-scale production molecular dynamics simulations are performed on selected interfaces under a range of thermodynamic conditions to elucidate interfacial phase transformation pathways.

1600 K,[7] in sharp contrast to diamond, which is only thermodynamically stable under high-pressure conditions. These observations underscore the fact that simple analogies with carbon are insufficient and highlight the need for a detailed atomistic understanding of the mechanisms governing phase transformations in BN.

Experimentally, phase transformations in BN are typically induced under high pressures and/or high temperatures.[10] More recently, however, alternative nonequilibrium synthesis techniques, such as nanosecond laser melting, spark plasma sintering, and high-energy mechanical ball milling, have emerged as viable routes for accessing metastable phases and transformation pathways that are inaccessible under equilibrium processing conditions.[11,12] Furthermore, intermediate polymorphs such as wBN and rBN are now recognized not only as transient states but also as structurally and functionally distinct materials with promising technological applications.[3,8,13−17] For example, wBN has attracted interest as a host material for quantum light emitters, while rBN is predicted to be the thermodynamically favored phase under typical chemical vapor deposition conditions.[3] These advances have shifted attention toward understanding the roles of kinetic pathways, defects, and local structural disorder in governing BN phase transformations, extending beyond the traditional equilibrium-based picture.

Theoretically, density functional theory (DFT), particularly with van der Waals-corrected and hybrid exchange-correlation functionals, has been widely used to investigate the thermodynamic stability, electronic structure, and static phase transformation energetics of BN polymorphs.[18−22] These approaches provide valuable insight into bulk phase behavior and the underlying physicochemical properties of BN. However, their computational cost limits their ability to describe kinetically controlled transformations over experimentally relevant length and time scales. Consequently, the atomistic mechanisms underlying phase evolution, including defect-mediated transformations, nucleation, atomic rearrangements, and lattice reconstruction, remain poorly understood. This gap hinders the identification and rational control of transformation pathways for achieving and stabilizing technologically relevant BN polymorphs. Addressing this challenge requires computational frameworks that retain near-first-principles accuracy while enabling simulations at the spatial and temporal scales necessary to resolve phase evolution dynamics.

Here, we address these challenges by extending a machine learning interatomic potential (MLIP)-assisted molecular dynamics workflow previously demonstrated by our group[23−25] to understand the BN polymorphic phase transformation mechanism. A MACE-based MLIP,[26,27] trained on high-fidelity *ab initio* data, enables simulations of BN polymorphs over length and time scales inaccessible to conventional *ab initio* molecular dynamics (AIMD) while retaining near-DFT accuracy. By tracking atomic trajectories

https://doi.org/10.1021/acs.jpclett.6c02892
J. Phys. Chem. Lett. 2026, 17, 13353−13360

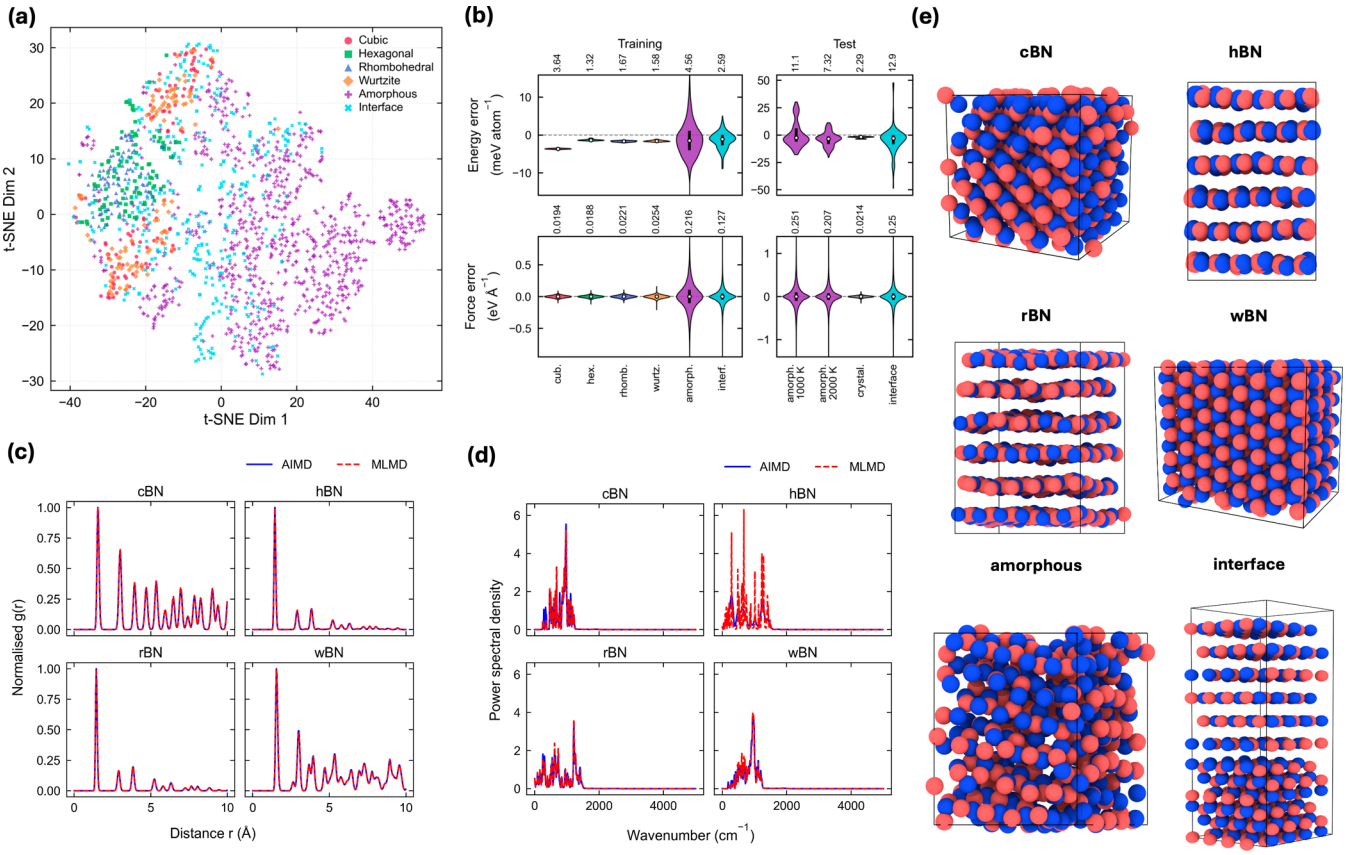

Figure 2. Performance and transferability validation of the trained MACE model across diverse BN structures. (a) t-SNE analysis of the configurational space represented by the training data set. (b) Energy and force error distributions (MACE-DFT) of the production model for the training and test data sets. Additional physical validations are performed by comparing (c) radial distribution functions (RDFs) and (d) vibrational power spectra obtained from AIMD and MLMD simulations. (e) Representative atomic configurations included in the training data set, encompassing crystalline, amorphous, and interfacial BN structures.

during machine learning-enabled molecular dynamics (MLMD) simulations under a range of thermodynamic conditions, we directly resolve phase transformation pathways and quantify how local atomic environments, interfacial energies, and internally generated stresses govern reconstructive phase evolution. This approach bridges atomistic mechanisms with macroscopic phase behavior, providing insight into the dynamic processes underlying BN polymorphism.

To construct an MLIP suitable for large-scale simulations of BN systems, we train a bespoke MACE model using a data set of uncorrelated configurations extracted from AIMD simulations spanning a wide range of thermodynamic conditions, crystal polymorphs, and local atomic environments. The predictive accuracy of the model, as well as its ability to reproduce key structural and dynamical properties, is rigorously validated through energy and force error distributions, radial distribution functions (RDFs), and vibrational power spectra (Figure 1, step 1). Next, we construct a diverse library of polymorphic BN interfaces, motivated by the expectation that phase transformations preferentially nucleated at interfaces due to their lower kinetic barriers. These interfacial structures are subsequently optimized with respect to both atomic positions and cell boundary conditions, yielding a ranked library of candidate systems for phase transformation studies (Figure 1, step 2). Finally, large-scale MLMD simulations are performed on selected interfaces under a range of thermodynamic conditions to directly probe phase transformation pathways and their associated energetics (Figure 1, step 3). Using this multilevel computational workflow, we resolve a layer-by-layer phase transformation mechanism initiated at polymorphic interfaces. The atomistic details are discussed below.

In step 1, the training data set was constructed by sampling a broad range of configurational space using AIMD under diverse thermodynamic conditions (Table S1 and Figure S1). Uncorrelated configurations are extracted from these trajectories and are subsequently labeled using single-point DFT calculations to obtain reference energies and forces. Following a two-tier validation and hyperparameter optimization procedure, the optimal MACE model was identified with l_{max} = 1 and c = 32 (Figure S2). A t-distributed stochastic neighbor embedding (t-SNE) analysis of the combined energy-per-atom and atomic force statistics for all training configurations (Figure 2a) reveals a clear separation between ordered crystalline and disordered amorphous structures. Principal component analysis (PCA) and uniform manifold approximation and projection (UMAP) results (Figure S3) also show the same trend, with crystalline polymorphs forming compact clusters and amorphous configurations occupying an extended high-force region. The resulting MLIP achieved root-mean-square errors (RMSEs) of 0.0037 eV per atom and 0.1680 eV Å^{-1} on the training set and 0.0100 eV per atom and 0.2076 eV Å^{-1} on the test set. The model also exhibited near-unity Pearson correlation coefficients, with ρ values of 0.9999 and

https://doi.org/10.1021/acs.jpclett.6c02892
J. Phys. Chem. Lett. 2026, 17, 13353−13360

0.9997 for the training and test energy predictions, respectively, and ρ values of 0.9962 and 0.9939 for the corresponding force predictions, demonstrating excellent agreement with the DFT reference data (Figure 2b).

The agreement on the test set demonstrates that the model is generalized beyond the training data, accurately predicting not only crystalline phases but also the more complex amorphous and interfacial configurations. The error distributions (MACE-DFT) of the eight MACE architectures are presented in Figures S4 and S5 and Table S2, illustrating the broad range of configurations represented in the training data set.

To further assess the fidelity of the MLIP, we compare RDFs (Figure 2c) and vibrational power spectra (Figure 2d) obtained from MLMD and AIMD simulations at 1000 K for the four crystalline BN polymorphs (Figure 2e) using the TRAVIS code.[28] As shown in Figure 2c, with the complete set of RDF comparisons provided in Figure S6, the MLIP accurately reproduces the peak positions and line shapes of all atomic pair correlations, including B−B, B−N, and N−N pairs across the BN polymorphs. This agreement demonstrates that the model captures both equilibrium bond lengths and thermally induced structural fluctuations. In cBN, the B−N, B−B, and N−N first-neighbor peaks (∼1.7, ∼2.5, and ∼2.7 Å, respectively) are matched within 0.02 Å, and second- and third-shell features up to ∼6−8 Å show a negligible phase shift, confirming preserved medium-range order. For layered hBN, the interlayer peak near ∼3.3 Å is well reproduced, capturing interlayer registry and hexagonal stacking l_{max}. Subtler features in rBN and wBN, such as the N−N second-shell splitting near 4.2−4.6 Å, are well captured, demonstrating accurate higher-order structural correlations.

The vibrational power spectra, obtained from the Fourier transform of mass-weighted velocity autocorrelation functions (Figure 2d), match AIMD results in peak positions, widths, and relative intensities. A complete set of power spectra are shown in Figure S7. The dominant cBN optical mode near ∼1200 cm^{-1} is reproduced with a negligible shift, while the layer-sensitive hBN modes (∼600−800 cm^{-1}) and the complex low-symmetry features of rBN and wBN (∼200−1000 cm^{-1}) are all captured with comparable spectral widths. The cumulative spectral integrals (Figure S7, right panels) agree within approximately 2% over the 0−5000 cm^{-1} range, further confirming accurate reproduction of the vibrational density of states. Together, these structural and vibrational validations demonstrate that the trained MLIP well reproduces both the local atomic environments and dynamical properties of BN polymorphs, establishing its reliability for investigating temperature-dependent behavior and phase transformation mechanisms.

In addition, across 55 strained configurations of four BN polymorphs (Figure S8), the MLIP reproduces DFT strain energies and stresses with MAEs of 3.5 meV/atom and 0.5 GPa, respectively. The largest deviations (20−27%) occur for out-of-plane deformation of layered hBN and rBN, suggesting that the bespoke MACE model has slightly reduced accuracy in capturing interlayer interactions that are governed by weak van der Waals forces, compared with the stronger covalent interactions within the atomic layers. DFT and MLIP also predict the same relative stability of the four BN polymorphs over the range of 0−20 GPa, with sub-meV per atom errors in their relative energies (Figure S9 and Tables S3−S5). Additional benchmark tests reveal that the current MLIP underestimates the formation energies of Schottky (vacancy) pairs by 7−11% and of antisite pairs by up to 24%. However, this does not limit the present study, as all production simulations are performed on stoichiometric systems and do not involve vacancy formation or undercoordinated defect environments (Figure S10 and Table S6). Figure S11 demonstrates direct DFT validation of configurations sampled around the phase transformation events showing excellent agreement with the MLIP in both energies and forces (force RMSE = 0.105 eV/Å; R^2 = 0.996). Collectively, the energy/force benchmarks, structural and vibrational comparisons, mechanical response tests, and relative thermodynamic phase stability of BN polymorphs demonstrate that the trained MLIP captures both near-equilibrium BN dynamics and the finite-strain response associated with B−N rearrangement, providing the basis for its application to the interfacial transformation simulations.

With the validated MLIP, we construct a library of BN interface structures to conduct MLMD simulations to investigate phase transformation mechanisms among different BN polymorphs. To identify the lowest-energy, nonpolar surface terminations for each BN phase, which serve as the building blocks for interfacial models, we employ pymatgen's `generate_all_slabs` routine to generate symmetry-distinct low-Miller index surface facets.[29] This procedure yields 4, 16, 7, and 11 candidate surface terminations for cBN, hBN, rBN, and wBN, respectively. The resulting slabs contain at least 2000 atoms with surface areas larger than 10 Å × 10 Å to ensure representative surface configurations. The surface energies are calculated using eq 1

$$\gamma_{surface} = \frac{E_{slab} - NE_{bulk}}{2A} \quad (1)$$

where E_{slab} is the total energy of the slab, E_{bulk} is the per atom energy of the corresponding bulk reference phase, N is the number of atoms in the slab, and A is the surface area. For asymmetric polar slabs, this expression yields the sum of the two complementary surface energies, and the reported value corresponds to their mean (details in section S10 of the Supporting Information). Among the surface configurations examined for each BN phase, those with the lowest surface energies for the low-index Miller indices are reported in Table 1.

To generate low-strain, lattice-matched interface models with favorable lateral registry, we employed the Canonicalized Affine-invariant Lattice Matching (CALM) code[30] and subsequently relaxed the structures using a consistent simulation protocol, as detailed in section S11. Following

Table 1. Ranked Low-Index Surfaces and Corresponding Surface Energies (joules per square meter) of the Four BN Polymorphs

polymorph	first stable	second stable	third stable
cBN	(110)	(111)	(100)
	3.30	5.98	9.11
hBN	(0001)	$(10\bar{1}1)$	$(11\bar{2}1)$
	0.06	1.74	3.70
rBN	(0001)	$(10\bar{1}0)$	$(11\bar{2}1)$
	0.06	3.21	3.78
wBN	$(10\bar{1}0)$	$(11\bar{2}0)$	$(11\bar{2}1)$
	2.60	2.87	4.89

https://doi.org/10.1021/acs.jpclett.6c02892
J. Phys. Chem. Lett. 2026, 17, 13353−13360

structural relaxation, the total interfacial energy was calculated with eq 2

$$\gamma_{\text{total}} = \frac{1}{2A}(E_{\text{AB}} - N_{\text{A}}E_{\text{A}}^{\text{bulk}} - N_{\text{B}}E_{\text{B}}^{\text{bulk}}) \quad (2)$$

where E_{AB} is the total energy of the relaxed interface, $E_{\text{A}}^{\text{bulk}}$ and $E_{\text{B}}^{\text{bulk}}$ are the per atom bulk energies of materials A and B, respectively, N_{A} and N_{B} are the corresponding numbers of atoms, and A is the interfacial area. The factor of 2 accounts for the two equivalent interfaces present in the periodic supercell.

Because coherent interface construction can introduce elastic strain into the model system, we further isolated the elastic contribution from the calculated interfacial energies. The elastic contribution, γ_{strain}, was obtained from oriented bulk cells constrained to the in-plane lattice dimensions of the corresponding interface while allowing relaxation normal to the interface. The intrinsic interfacial energy was then defined with eq 3.

$$\gamma_{\text{interface}} = \gamma_{\text{total}} - \gamma_{\text{strain}} \quad (3)$$

Three lowest-energy converged interface structures for each BN polymorph pair are reported in Table 2, and the complete set of interfacial energies, γ, for all 54 configurations of each polymorph pair is reported in Table S7. The elastic contribution is small (<20%) and has little effect on the overall interface energy trends, which are primarily governed by local interfacial chemistry and bonding. These optimized interfaces represent the thermodynamically preferred registries for their respective polymorph combinations and span a representative range of stacking, rotational, and translational arrangements that influence the early stages of phase transformation.

Table 2. Three Lowest-Energy Converged Interface Structures for Each BN Polymorph Pair[a]

interface pair	rank	orientation	γ_{total}	γ_{strain} (J/m^2)	$\gamma_{\text{interface}}$
cBN−hBN	first	110−0001	3.24	0.03	3.21
	second	110−10$\bar{1}$1	5.06	0.17	4.89
	third	111−0001	5.51	0.26	5.25
cBN−rBN	first	110−0001	3.22	0.03	3.19
	second	111−0001	5.55	0.14	5.40
	third	110−11$\bar{2}$1	6.78	0.18	6.60
cBN−wBN	first	110−10$\bar{1}$0	5.62	0.03	5.60
	second	110−11$\bar{2}$0	5.96	0.02	5.94
	third	111−11$\bar{2}$0	7.33	0.51	6.82
hBN−rBN	first	0001−0001	0.12	0.00	0.11
	second	10$\bar{1}$1−0001	1.77	0.11	1.66
	third	0001−11$\bar{2}$1	3.52	0.10	3.42
hBN−wBN	first	0001−10$\bar{1}$0	2.51	0.05	2.46
	second	0001−11$\bar{2}$0	2.89	0.11	2.78
	third	10$\bar{1}$1−10$\bar{1}$0	4.24	0.12	4.12
rBN−wBN	first	0001−10$\bar{1}$0	2.58	0.06	2.52
	second	0001−11$\bar{2}$0	2.88	0.11	2.77
	third	0001−11$\bar{2}$1	5.37	0.14	5.23

[a]The total interfacial energy, strain contribution, and strain-corrected interfacial energy (γ_{total}, γ_{strain}, and $\gamma_{\text{interface}}$, respectively) are given in joules per square meter. The complete set of obtained interfacial energy for all 54 interface model is provided in Table S7.

For the down-selected interface systems, MLMD simulations were performed using LAMMPS[31] with the trained MLIP (see Computational Methods in the Supporting Information for the complete simulation setup). The MLMD simulations reveal a pronounced interface-driven, layer-by-layer phase transformation in BN, as illustrated in Figure 3. Specifically, for the cBN−hBN interface (Figure 3a), during thermal equilibration under *NVT* at 300 K, followed by *NPT* at 1 bar, the interface remains structurally stable.

Upon heating from 300 to 1000 K, local lattice distortions develop at the interface, initiating a layer-by-layer structural transformation in which the sp^3-bonded B−N configuration characteristic of the cBN phase is progressively converted into the sp^2-bonded B−N network, leading to hBN phase formation.

A similar layer-resolved transformation mechanism is observed for the hBN(0001)−wBN(10$\bar{1}$0) interface (Figure 3c), although it is preceded by more pronounced interfacial fluctuations. During *NPT* equilibration, the wBN layers already exhibit significant out-of-plane buckling. Upon heating, these fluctuations are intensified, ultimately inducing bond reorientation in the layers adjacent to the interface. The phase transformation then propagates layer by layer through sequential flattening of the buckled wBN layers into planar hBN sheets, as shown in Figure 3c. The buckling period equals the lateral period of the simulation cell, the longest wavelength the periodic cell can accommodate, and should therefore not be interpreted as the intrinsic buckling wavelength. Importantly, the first single-layer conversion is reproduced in a laterally doubled, 14 400-atom cell (section S13). This local flattening motif is consistent with mechanisms previously proposed from shock-compression and high-temperature studies of wBN-to-layered-BN transformations.[32,33] In contrast, the cBN(111)−wBN(10$\bar{1}$0) (Figure 3b) and rBN(0001)−wBN(11$\bar{2}$0) (Figure 3d) interface systems do not undergo phase transformation within the timescale sampled by the MLMD simulations, indicating that the corresponding reconstruction pathway was not accessed on the nanosecond timescale. Assuming an attempt frequency of 10^{13} s^{-1}, the absence of an event corresponds to an approximate lower bound of ∼0.8 eV for effective barrier (see section S11.1 for details). In addition, the two systems exhibit distinct interfacial dynamics. The cBN(111)−wBN(10$\bar{1}$0) interface remains structurally stable throughout the simulation, whereas the rBN(0001)−wBN(11$\bar{2}$0) interface develops significant structural fluctuations and large-amplitude lattice distortions without evolving into a well-defined layer-by-layer transformation.

Overall, this BN transformation behavior cannot be described by interfacial energy alone. Layer-resolved analysis (section S11.2, Figure S12 and Table S8) shows that the transforming interfaces contain interfacial B atoms with B−N bonds along the interface normal that are prestretched to approximately 1.70 Å, facilitating rearrangement toward a planar B−N bonding configuration. This motif is absent at the rBN(0001)−wBN(11$\bar{2}$0) interface, while the cBN(111)−wBN(10$\bar{1}$0) interface lacks a compliant wBN phase to accommodate the converted layer. A registry-controlled test on the cBN(111)−hBN(0001) interface (section S14 and Figure S16) further demonstrates that interfacial energy cannot serve as a single descriptor of BN phase evolution behavior. All newly constructed interface structures exhibit comparable interfacial energies but substantially different upper bounds on the barriers for flattening of the outermost cBN bilayer at the interface, ranging from 0 to approximately 1 eV. This barrier correlates strongly with local registry (R^2 = 0.74), but not with

https://doi.org/10.1021/acs.jpclett.6c02892
J. Phys. Chem. Lett. 2026, 17, 13353−13360

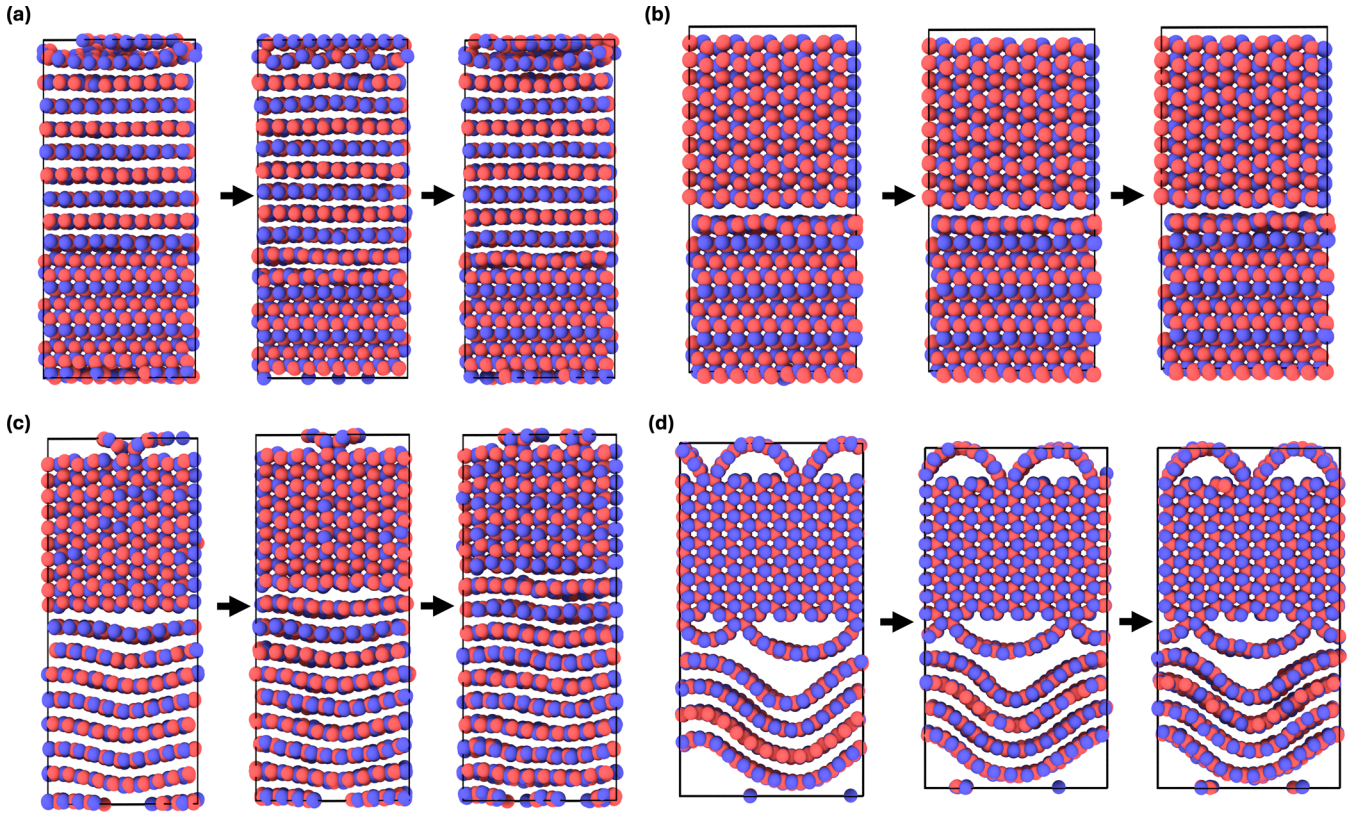

Figure 3. Layer-by-layer phase transformation behavior of BN revealed by MLMD simulations. Structural representations are shown for (a) cBN(111)−hBN(0001), (b) cBN(111)−wBN(10$\bar{1}$0), (c) hBN(0001)−wBN(10$\bar{1}$0), and (d) rBN(0001)−wBN(11 $\bar{2}$0) interface systems. All simulations were performed under identical thermodynamic conditions (see Simulation Details in the Supporting Information).

mean interlayer distance (R^2 = −0.07). Taken together, these analyses indicate that crystallographic orientation, local bonding topology, interfacial registry, and kinetic accessibility collectively govern whether the transformation proceeds.

To quantitatively characterize the layer-by-layer interfacial phase transformation observed visually, we analyzed the evolution of local B−N coordination throughout the MLMD trajectories. The layer-resolved coordination analyses (Figure S13) show that both interfaces undergo distinct, discrete layer-by-layer reconstruction, rather than continuous interfacial evolution involving disordered, mixed sp^3/sp^2 states. The phase boundary remains nearly stationary between transformation events and advances by approximately one structural layer during each interfacial reconstruction event. This stepwise behavior is reproduced in independent trajectories with different random seeds and heating rates, which yield the same number of discrete conversion steps and the same final 4-fold fraction (Table S9 and Figure S14). No detectable populations of undercoordinated or overcoordinated atoms develop within the simulation timescale, supporting a predominantly crystalline-to-crystalline transformation pathway without the formation of a long-lived amorphous intermediate. Further increasing the system size by doubling the lateral dimensions of the interface reconfirms the evolution of local B−N coordination during the interfacial phase transformation (Table S10 and Figure S15).

The pressure evolution provides complementary insight into the mechanical response accompanying these transformations (Figure S17). In all systems, the total pressure (P_{tot}) approaches zero during *NPT* equilibration, indicating a mechanically relaxed state, consistent with the near-zero pressure observed for the stable stacking configurations. As the temperature increases, P_{tot} becomes progressively positive, corresponding to the buildup of compressive stress. This increase in pressure coincides with the onset of structural transformation observed in Figure 3. The resulting anisotropic interfacial stress, arising from thermal expansion mismatch and interfacial constraints, may modify the kinetic accessibility of local atomic rearrangements as evidenced by the increasing pressure profiles in Figure S17a−c. The directional evolution of the anisotropic pressure components (P_{xx}, P_{yy}, and P_{zz}) reveals that compressive stress develops preferentially along specific crystallographic directions, promoting structural reconstruction along the interface normal and enabling the sequential, layer-by-layer transformation observed in Figure 3 occurring at ∼1.8 and ∼4.1 ns (Figure S13a). For the hBN(0001)−wBN(10$\bar{1}$0) system, the out-of-plane buckling of the wBN layers is accompanied by fluctuations in the pressure components (Figure S17g−i), and the transformation occurs within well-defined temporal windows (e.g., ∼3.8 and ∼4.7 ns), indicating that the process is governed by local activation barriers rather than occurring continuously (Figure S13b).

Compressive pressure alone, however, is insufficient to induce phase transformation. For the cBN(110)−wBN(10$\bar{1}$0) interface, a comparable increase in compressive pressure develops during heating (Figure S17d−f), yet the atomic structure remains stable throughout the simulation. This behavior suggests that crystallographic orientation and interfacial geometry play a decisive role. The bonding network in this configuration is less susceptible to distortion, and the applied stress is insufficient to overcome the higher activation barrier for structural reconstruction. Likewise, the

https://doi.org/10.1021/acs.jpclett.6c02892
J. Phys. Chem. Lett. 2026, 17, 13353−13360

rBN(0001)−wBN(11$\bar{2}$0) interface accommodates the accumulated compressive stress (Figure S17j−l) primarily through large-amplitude lattice distortions rather than a cooperative layer-by-layer transformation. These results demonstrate that thermally generated interfacial stress can modify the kinetic accessibility of structural reconstruction but does not provide the bulk thermodynamic driving force for the cBN-to-hBN transformation that involves a volume expansion and is rather unfavorable under compression. Whether a phase transformation occurs is therefore governed by structural compatibility and the availability of kinetically accessible transformation pathways.

In summary, we extended a MLMD framework based on an in-house trained MACE MLIP to investigate phase transformation mechanisms among BN polymorphs. The trained MLIP shows excellent agreement with DFT calculations and AIMD simulations in reproducing the structural and vibrational properties of the cubic, hexagonal, rhombohedral, and wurtzite BN phases, demonstrating both its accuracy and transferability for large-scale atomistic simulations. Our simulations reveal that phase transformation in BN is governed by a complex interplay among interfacial energetics, thermal activation, and local atomic structure. In particular, we show that phase transformations are initiated at interfaces and propagate through a layer-resolved mechanism, where lattice mismatch and local structural disorder create favorable nucleation sites for bond rearrangement. Thermally generated anisotropic interfacial stress can modify the kinetic accessibility of structural reconstruction but is not interpreted as the bulk thermodynamic driving force for conversion toward layered hBN. Crystallographic compatibility and the availability of kinetically accessible atomic pathways ultimately determine whether reconstruction can proceed. These findings establish interfacial energetics and local structural compatibility as key factors governing phase stability and transformation pathways in BN polymorphs, providing atomistic insights for the rational design and synthesis of metastable BN materials.

■ ASSOCIATED CONTENT

Supporting Information

The Supporting Information is available free of charge at https://pubs.acs.org/doi/10.1021/acs.jpclett.6c02892.

Additional computational details (section S1) and MLIP validation; training data set and model evaluation (sections S2−S5); strain, equation of state (section S6), polymorph stability (section S7), defect (section S8), and transformation−configuration benchmarks (section S9); surface and interface energetics (sections S10 and S11); local structure and layer-resolved analyses of phase transformations (section S12); statistical robustness and interfacial registry tests (sections S13 and S14); and pressure evolution from MLMD results (section S15) (PDF)

■ AUTHOR INFORMATION

Corresponding Authors

Nikhil Rampal − *Materials Science Division and Laboratory for Energy Applications for the Future (LEAF), Lawrence Livermore National Laboratory, Livermore, California 94550, United States;* orcid.org/0000-0003-2143-5874; Email: rampal1@llnl.gov

Liwen F. Wan − *Materials Science Division and Laboratory for Energy Applications for the Future (LEAF), Lawrence Livermore National Laboratory, Livermore, California 94550, United States;* orcid.org/0000-0002-5391-0804; Email: wan6@llnl.gov

Authors

Jaeyoung Cho − *Department of Chemistry, The University of Texas at Austin, Austin, Texas 78712, United States; Materials Science Division, Lawrence Livermore National Laboratory, Livermore, California 94550, United States*

Stephen E. Weitzner − *Materials Science Division and Laboratory for Energy Applications for the Future (LEAF), Lawrence Livermore National Laboratory, Livermore, California 94550, United States;* orcid.org/0000-0002-9278-5073

Graeme Henkelman − *Department of Chemistry and Oden Institute for Computational Engineering & Sciences, The University of Texas at Austin, Austin, Texas 78712, United States;* orcid.org/0000-0002-0336-7153

Complete contact information is available at: https://pubs.acs.org/10.1021/acs.jpclett.6c02892

Notes

The authors declare no competing financial interest.

■ ACKNOWLEDGMENTS

This work was performed under the auspices of the U.S. Department of Energy by Lawrence Livermore National Laboratory under Contract DE-AC52-07NA27344 and was supported by the Laboratory Directed Research and Development funding under Project 22-ERD-049. Computing resources were provided partially by the Computing Grand Challenge program at Lawrence Livermore National Laboratory and facilities sponsored by the U.S. Department of Energy's Office of Critical Minerals and Energy Innovation and located at the National Laboratory of the Rockies. The computing resources in Austin was supported by the Texas Advanced Computing Center.

■ REFERENCES

(1) Chen, S.-H.; Magyari-Kope, B.; Hsu, C.-H.; Woon, W.-Y.; Liao, S. S. Boron Nitride for Applications in Microelectronics. *Nature Reviews Electrical Engineering* **2025**, *2*, 205−214.

(2) Moon, S.; et al. Hexagonal Boron Nitride for Next-Generation Photonics and Electronics. *Adv. Mater.* **2023**, *35*, 2204161.

(3) Çakan, A.; et al. Quantum Optics Applications of Hexagonal Boron Nitride Defects. *Adv. Opt. Mater.* **2025**, *13*, 2402508.

(4) Wu, Y.; et al. Defect-Engineered Hexagonal Boron Nitride EnablesIonic Conduction for Lithium Metal Batteries. *Nano Lett.* **2026**, *26*, 9791−9800.

(5) Chen, K.; et al. Ultrahigh Thermal Conductivity in Isotope-Enriched Cubic Boron Nitride. *Science* **2020**, *367*, 555−559.

(6) Biswas, A.; et al. Phase Stability of Hexagonal/Cubic Boron Nitride Nanocomposites. *Nano Lett.* **2023**, *23*, 6927−6936.

(7) Biswas, A.; et al. Cubic and Hexagonal Boron Nitride Phases and Phase Boundaries. *Journal of Materials Chemistry C* **2024**, *12*, 3053−3062.

(8) Pedersen, H.; Alling, B.; Högberg, H.; Ektarawong, A. Thermodynamic Stability of Hexagonal and Rhombohedral Boron Nitride under Chemical Vapor Deposition Conditions from van Der Waals Corrected First Principles Calculations. *J. Vac. Sci. Technol., A* **2019**, *37*, 040603.

(9) Solozhenko, V. L.; Turkevich, V. Z.; Holzapfel, W. B. Refined Phase Diagram of Boron Nitride. *J. Phys. Chem. B* **1999**, *103*, 2903−2905.
(10) Singh, B.; Nover, G.; Will, G. High Pressure Phase Transformations of Cubic Boron Nitride from Amorphous Boron Nitride Using Magnesium Boron Nitride as the Catalyst. *J. Cryst. Growth* **1995**, *152*, 143−149.
(11) Narayan, J.; Bhaumik, A. Research Update: Direct Conversion of h-BN into Pure c-BN at Ambient Temperatures and Pressures in Air. *APL Mater.* **2016**, *4*, 020701.
(12) Batsanov, S. S.; Gavrilkin, S. M.; Bezduganov, S. V.; Romanov, P. N. Reversible Phase Transformation in Boron Nitride under Pulsed Mechanical Action. *Inorg. Mater.* **2008**, *44*, 1199−1201.
(13) Silvetti, M.; Pouyot, M.; Cannuccia, E. Wurtzite Boron Nitride as a Potential Defects Host. *arXiv* **2025**, DOI: 10.48550/arXiv.2506.21197.
(14) Wang, L.; et al. Bevel-Edge Epitaxy of Ferroelectric Rhombohedral Boron Nitride Single Crystal. *Nature* **2024**, *629*, 74−79.
(15) Gale, A.; et al. Quantum Emitters in Rhombohedral Boron Nitride. *Adv. Opt. Mater.* **2025**, *13*, e00593.
(16) Silvetti, M.; Attaccalite, C.; Cannuccia, E. Pressure Dependence of Electronic, Vibrational and Optical Properties of Wurtzite-Boron Nitride. *Physical Review Materials* **2023**, *7*, 055201.
(17) Olovsson, W.; Magnuson, M. Rhombohedral and Turbostratic Boron Nitride Polytypes Investigated by X-Ray Absorption Spectroscopy. *J. Phys. Chem. C* **2022**, *126*, 21101−21108.
(18) Dreyer, C. E.; Lyons, J. L.; Janotti, A.; Van De Walle, C. G. Band Alignments and Polarization Properties of BN Polymorphs. *Applied Physics Express* **2014**, *7*, 031001.
(19) Yu, W. J.; Lau, W. M.; Chan, S. P.; Liu, Z. F.; Zheng, Q. Q. *Ab Initio* Study of Phase Transformations in Boron Nitride. *Phys. Rev. B* **2003**, *67*, 014108.
(20) Cazorla, C.; Gould, T. Polymorphism of Bulk Boron Nitride. *Sci. Adv.* **2019**, *5*, eaau5832.
(21) Marom, N.; et al. Stacking and Registry Effects in Layered Materials: The Case of Hexagonal Boron Nitride. *Phys. Rev. Lett.* **2010**, *105*, 046801.
(22) Nikaido, Y.; et al. Diffusion Monte Carlo Study on Relative Stabilities of Boron Nitride Polymorphs. *J. Phys. Chem. C* **2022**, *126*, 6000−6007.
(23) Bunting, R. J.; et al. Direct Ab Initio Simulation of the Synthesis of $BaZrO_3$ and the Microstructure Impacts on Proton Transport. *ACS Nano* **2026**, *20*, 15181−15189.
(24) Rampal, N.; et al. Physics-Informed Machine Learning Exploration of Na Storage Mechanisms in Disordered Carbon. *Energy Storage Materials* **2026**, *86*, 104967.
(25) Yuan, S.; Rampal, N.; Adelstein, N.; Wan, L. F. Elucidating Lithium Transport Mechanisms in Disordered LiF from Machine-Learning Molecular Dynamics Simulations. *ACS Materials Letters* **2026**, *8*, 1833−1838.
(26) Batatia, I.; et al. The Design Space of E(3)-Equivariant Atom-Centred Interatomic Potentials. *Nature Machine Intelligence* **2025**, *7*, 56−67.
(27) Batatia, I.; et al. A Foundation Model for Atomistic Materials Chemistry. *J. Chem. Phys.* **2025**, *163*, 184110.
(28) Brehm, M.; Thomas, M.; Gehrke, S.; Kirchner, B. TRAVIS−A Free Analyzer for Trajectories from Molecular Simulation. *J. Chem. Phys.* **2020**, *152*, 164105.
(29) Ong, S. P.; et al. Python Materials Genomics (Pymatgen): A Robust, Open-Source Python Library for Materials Analysis. *Comput. Mater. Sci.* **2013**, *68*, 314−319.
(30) Adelstein, N.; Holber, J. E.; Rampal, N.; Weitzner, S. E. *The Canonicalized Affine-invariant Lattice Matching Code for Interface Modeling*, 2026. https://github.com/llnl/calm (2026, August 01).
(31) Thompson, A. P.; et al. LAMMPS − a Flexible Simulation Tool for Particle-Based Materials Modeling at the Atomic, Meso, and Continuum Scales. *Comput. Phys. Commun.* **2022**, *271*, 108171.
(32) Britun, V.; Kurdyumov, A.; Petrusha, I. Wurtzitic Boron Nitride Thermal Stability and Transformation into the Rhombohedral Boron Nitride Modification When Heated. *Mater. Lett.* **1999**, *41*, 83−88.
(33) Britun, V. F.; Kurdyumov, A. V. Mechanisms of Martensitic Transformations in Boron Nitride and Conditions of Their Development. *High Pressure Research* **2000**, *17*, 101−111.

https://doi.org/10.1021/acs.jpclett.6c02892
J. Phys. Chem. Lett. 2026, 17, 13353−13360